Article

Fast Ionic Migration from Bulk to Interface in the Li(NH$_3$)$_x$BH$_4$@SiO$_2$ Composite

Zhenhua Liu, Tengfei Zhang,* Shunlong Ju, Yanda Ji, Zhaotong Hu, Yingtong Lv, Guanglin Xia, and Xuebin Yu*

Cite This: *ACS Appl. Energy Mater.* 2022, 5, 14301−14310

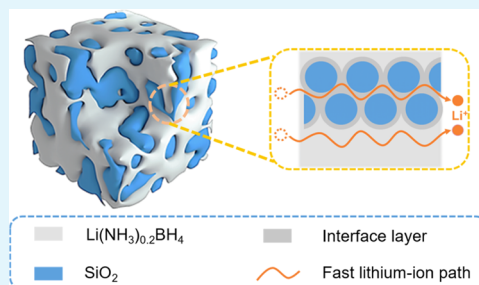Read Online

ACCESS | Metrics & More | Article Recommendations | Supporting Information

ABSTRACT: Lithium borohydride (LiBH$_4$), with high compatibility to lithium anode, low grain boundary resistance, and light mass, is regarded as a promising solid-state electrolyte. However, poor ionic conductivity at room temperature limits its practical application in all-solid-state lithium-ion batteries (ASSLBs). In the present study, Li(NH$_3$)$_x$BH$_4$@SiO$_2$ ($0 \leq x \leq 0.5$) composites were obtained by ammonia absorption and simple ball-milling. Among them, Li(NH$_3$)$_{0.5}$BH$_4$@ SiO$_2$ exhibits a high ionic conductivity of 3.95×10^{-2} S cm^{-1} at 60 °C, with a lithium transference number up to 0.9999 at 30 °C. More importantly, the experimental results and density functional theory (DFT) calculations show that the skeleton and interfacial interaction of silica can effectively improve the electrochemical performance of the full cell. All-solid-state lithium−sulfur batteries exhibit a specific discharge capacity of 1221.7 mAh g^{-1} after 10 cycles. Reversible capacities of 1589, 1381, 1176, 969, and 695 mAh g^{-1} could be achieved at 0.1, 0.2, 0.3, 0.5, and 1C, respectively. These findings prove that Li(NH$_3$)$_x$BH$_4$@SiO$_2$ is an attractive electrolyte for next-generation ASSLBs.

KEYWORDS: *all-solid-state lithium-ion batteries, lithium borohydride, ionic conductivity, density functional theory, sulfurized polyacrylonitrile cathodes*

Legend: Li(NH$_3$)$_{0.2}$BH$_4$ | Interface layer | SiO$_2$ | Fast lithium-ion path

INTRODUCTION

All-solid-state lithium-ion batteries (ASSLBs) with solid-state electrolytes (SSEs) are considered as promising alternatives to traditional lithium-ion batteries. Compared with liquid electrolytes, SSEs have better chemical stability, lower electronic conductivity, and higher mechanical strength.[1−4] The solid structure makes ion migration more stable, actualizing uniform lithium deposition during battery cycles.[5] Then, the risk of short circuits caused by lithium dendrites is decreased.[6−8] Furthermore, matching solid electrolytes with a lithium metal anode and a high-voltage cathode can not only improve the energy density but also overcome safety issues. Significant attention has therefore been paid to the development of SSEs with excellent performance for the current energy storage field.[9−11]

For the last 2 decades, researchers have made significant progress in the study of various electrolyte systems, such as polymers,[12−16] oxides,[17−21] sulfides,[22−27] hydrides,[28−33] and halides.[34−38] Among them, hydride-based electrolytes have the advantages of good reduction stability to lithium, excellent mechanical properties, and low grain boundary resistance.[2,39] However, in the lithium borohydride electrolyte, lithium ions can only conduct rapidly in the high-temperature phase, which seriously restricts the application of lithium borohydride at moderate temperatures. Significant efforts have been made to improve the ionic conductivity of LiBH$_4$, such as second-phase
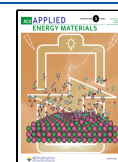
compositions,[40−46] anion doping,[26,28,30,31,47,48] and nano-confined modifications.[29,49−52] More recently, the crystal structure of lithium borohydride has been enlarged by the introduction of ammonia gas, leading to a decrease in the activation energy of Li-ion migration.[53] As the temperature increases, the conductivity of Li(NH$_3$)BH$_4$ increases drastically (2.21×10^{-3} S cm^{-1} at 40 °C). However, as the temperature continually increases to 50 °C, Li(NH$_3$)$_x$BH$_4$ ($0 < x \leq 1$) partially starts melting. The conductivity increases with an increase in the amount of ammonia, but the solid−liquid transition temperature decreases.[54] This special property limits the use of lithium borohydride ammoniates in SSEs. Meanwhile, choosing the appropriate cathode to assemble a full cell has baffled researchers.[55,56]

In this study, we designed a composite material composed of lithium borohydride ammoniates (Li(NH$_3$)$_x$BH$_4$ as cement) and silicon dioxide (SiO$_2$ nanoparticles as bricks) to achieve both high ionic conductivity and structural stability of the electrolyte (Figure 1a). This was achieved simply by ball-

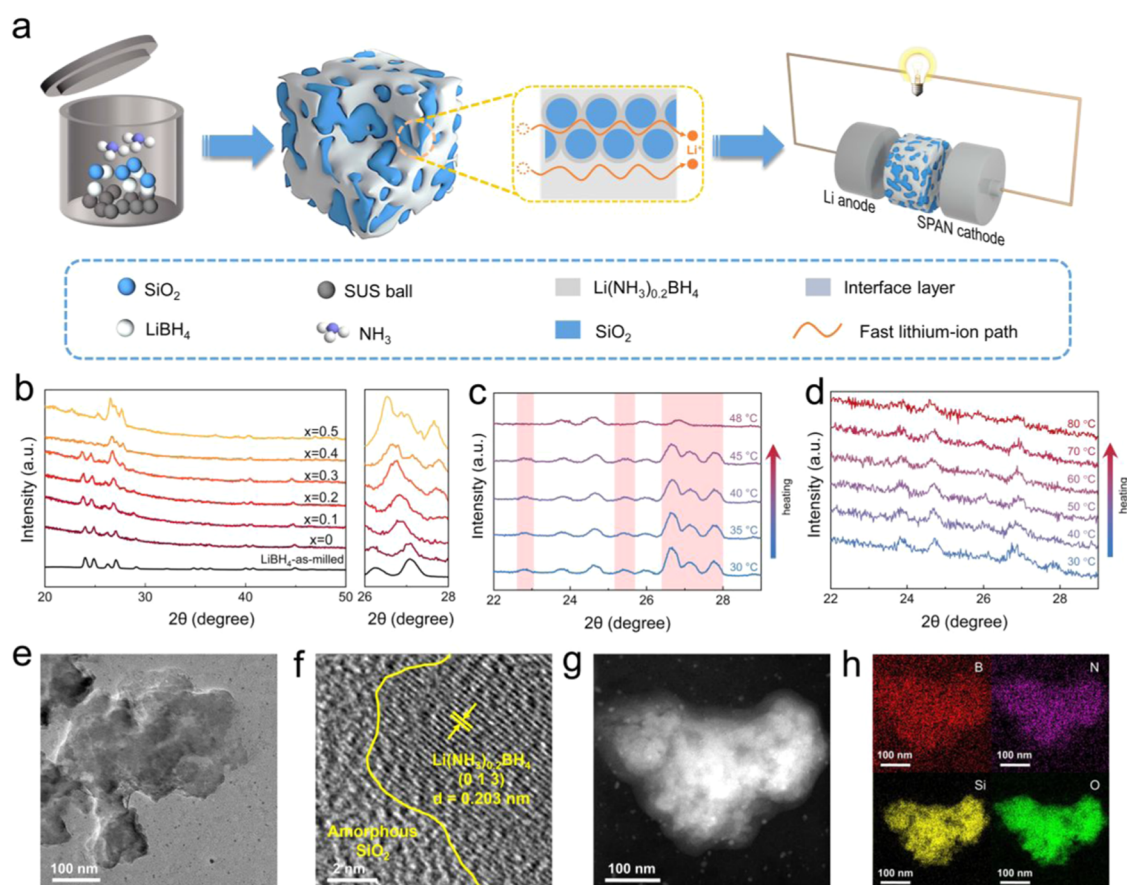**Figure 1.** (a) Schematic illustration of the electrolyte synthesis and an integrated all-solid-state $Li/Li(NH_3)_{0.2}BH_4@SiO_2/SPAN$ battery. (b) XRD patterns of $LiBH_4$ and $Li(NH_3)_xBH_4@SiO_2$. (c) In situ XRD patterns of $Li(NH_3)_{0.2}BH_4$ during the heating process. (d) In situ XRD patterns of $Li(NH_3)_{0.2}BH_4@SiO_2$ during the heating process. (e, f) TEM and HRTEM images of $Li(NH_3)_{0.2}BH_4@SiO_2$. (g, h) HAADF image and corresponding EDS mapping of $Li(NH_3)_{0.2}BH_4@SiO_2$.

milling and absorbing ammonia, leading to the formation of fast lithium ion migration pathways ($Li(NH_3)_{0.2}BH_4$ bulk phase and interface phase). Both experimental results and DFT calculations reveal that a small diffusion barrier and fast migration pathways are acquired from the composite, which leads to superior conductivity. The electrochemical performance of the Li−S full cell was also investigated based on the $Li(NH_3)_{0.2}BH_4@SiO_2$ electrolyte.

RESULTS AND DISCUSSION

Material Characterizations. Figure 1b shows the X-ray diffraction (XRD) patterns of $LiBH_4$ and $Li(NH_3)_xBH_4@SiO_2$ (x = 0, 0.1, 0.2, 0.3, 0.4, 0.5) composites at room temperature (XRD pattern of fumed SiO_2 is shown in Figure S1). Before measurement, $LiBH_4$ was preprocessed under the same ball-milling conditions as those of $Li(NH_3)_xBH_4@SiO_2$. The XRD pattern of fumed SiO_2 does not show diffraction patterns because of its amorphous state. Ball-milling with SiO_2 would reduce the crystallinity of lithium borohydride ammoniates. When the stoichiometric ratio of ammonia to lithium borohydride increases from 0 to 0.3, the crystal structure of the composite does not change significantly, only resulting in a small left shift of the overall diffraction patterns from the enlarged figure. The ammoniated phase forms between 22 and 28°. The crystal structure of the composite changes with an increase in the amount of ammonia above 0.5, where the lithium borohydride phase starts to transform completely into

the ammoniated phase. Therefore, a stoichiometric ratio of 0.5 is considered as the phase transition point. Furthermore, the (1 1 1) lattice spacing of each sample is calculated by the Bragg formula, listed in Table S1. For instance, the lattice spacing of the $LiBH_4@SiO_2$ composite at (1 1 1) is 3.292 Å, which is the same as that of as-milled $LiBH_4$. However, when the ratio of x increases to 0.1, 0.2, and 0.3, the lattice spacing of the $Li(NH_3)_xBH_4@SiO_2$ composite increases to 3.320, 3.323, and 3.330 Å, respectively. The lattice spacing of the composite increases with the increased absorption of ammonia, indicating the expansion of the unit cell volume of $Li(NH_3)_xBH_4$.[54,57] Taking $Li(NH_3)BH_4$ as an example, its unit cell volume is about 1.8 times that of $LiBH_4$, as shown in Table S2. This will reduce the volume density of lithium ions and enhance the transport of lithium ions.[53] Then, in situ XRD analysis was performed to understand the structural stability. Figure 1c,d shows the in situ XRD patterns corresponding to $Li(NH_3)_{0.2}BH_4$ and $Li(NH_3)_{0.2}BH_4@SiO_2$ composites at various temperatures. As a result of high-energy ball milling and the presence of amorphous silica, the intensity of the $Li(NH_3)_{0.2}BH_4@SiO_2$ phase in Figure 1d is weak, but the diffraction peak positions of the two phases are consistent. The crystal structure partially changes from the $Li(NH_3)_{0.2}BH_4$ composite to $Li(NH_3)_xBH_4$ ($0 < x < 0.2$), and the sample pellet melts at the same time when the temperature increases to 48 °C. As ammonia escaped from the crystal structure, the characteristic peak of lithium borohydride ammoniate
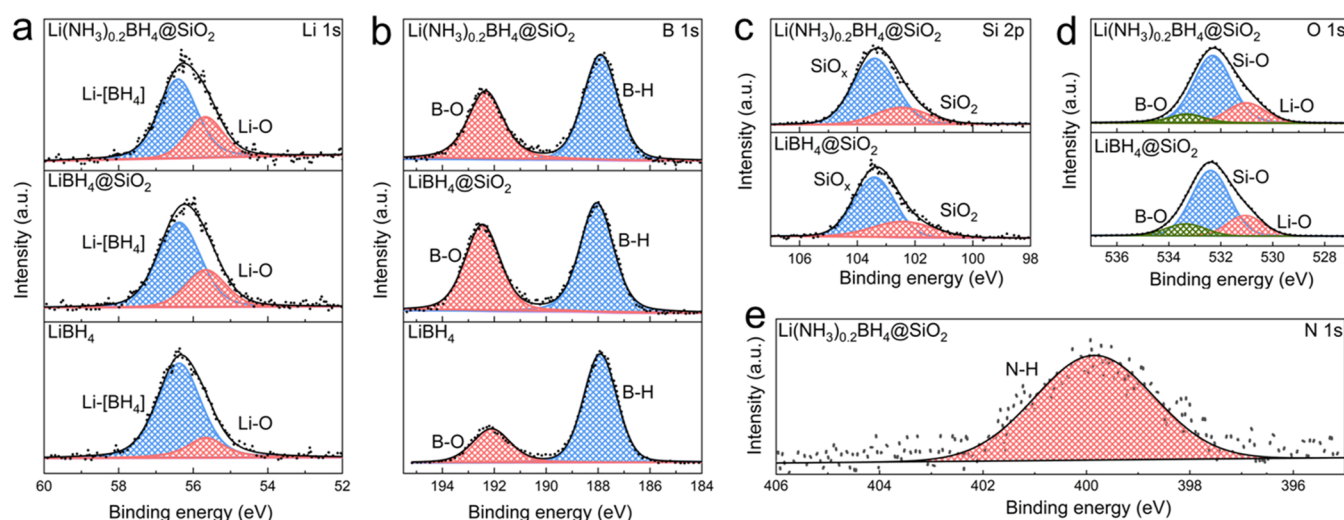
Figure 2. (a) Li 1s and (b) B 1s XPS spectra of $LiBH_4$, $LiBH_4@SiO_2$, and $Li(NH_3)_{0.2}BH_4@SiO_2$. (c) Si 2p and (d) O 1s XPS spectra of $LiBH_4@SiO_2$ and $Li(NH_3)_{0.2}BH_4@SiO_2$. (e) N 1s XPS spectrum of $Li(NH_3)_{0.2}BH_4@SiO_2$.
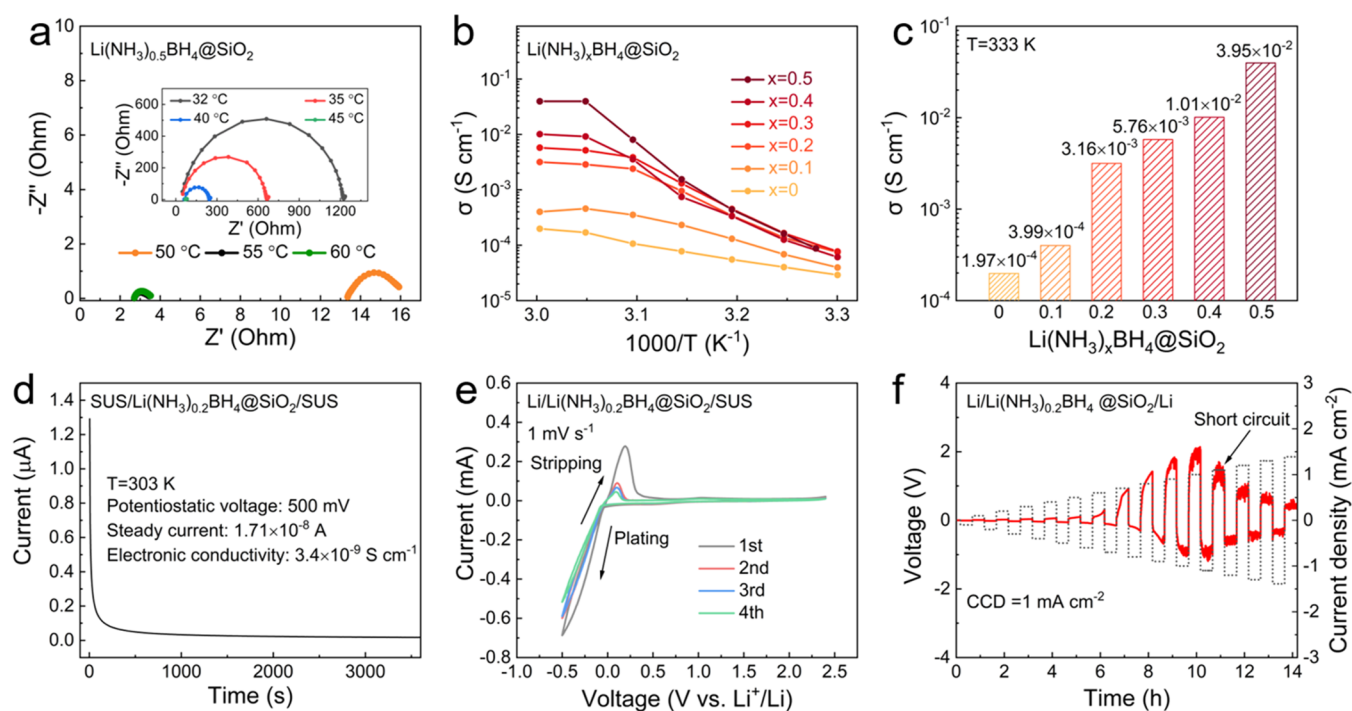

Figure 3. (a) Typical Nyquist curves of $Li(NH_3)_{0.5}BH_4@SiO_2$ at different temperatures. (b) Arrhenius plots of $Li(NH_3)_xBH_4@SiO_2$. (c) Lithium ionic conductivity of $Li(NH_3)_xBH_4@SiO_2$ at 333 K. (d) DC polarization curve of $Li(NH_3)_{0.5}BH_4@SiO_2$ at 303 K. (e) CV curves of $Li(NH_3)_{0.2}BH_4@SiO_2$ at 313 K. (f) Galvanostatic cycling curves of the $Li/Li(NH_3)_{0.2}BH_4@SiO_2/Li$ symmetric cell at increasing current densities.

disappeared. However, the structure of the $Li(NH_3)_{0.2}BH_4@SiO_2$ composite was retained after heating at 80 °C. The peak position did not present obvious differences compared with that at 30 °C; only the intensity decreased as the ammonia partially desorbed. As a result, the introduction of SiO_2 can effectively improve the thermal stability of the electrolyte structure.

The morphology of the $Li(NH_3)_{0.2}BH_4@SiO_2$ composite is further observed by transmission electron microscopy (TEM) (Figure 1e). The bright-field image of SiO_2 is shown in Figure S2a, which exhibits a spherical morphology with a particle size of less than 15 nm. As a result of the impact of the shear force during ball-milling, the $Li(NH_3)_{0.2}BH_4@SiO_2$ composite forms

agglomerated particles and irregular shapes. As shown in Figure 1f, both crystalline and amorphous phases are observed in the high-resolution transmission electron microscopy (HRTEM) image, identifying the (0 1 3) lattice plane of $Li(NH_3)_{0.2}BH_4$ and SiO_2, respectively. Good contact between the borohydride and insulating nanoparticles was also confirmed.[58] Figure 1g,h shows the high-angle annular dark-field (HAADF) image and corresponding energy-dispersive X-ray spectroscopy (EDS) mapping of the composite. The homogeneous distribution of N and B indicates that ammonia has been uniformly absorbed into the lattice of $LiBH_4$. Similar distribution results were also observed for the $LiBH_4@SiO_2$ composite, as presented in Figure S2. In addition, the

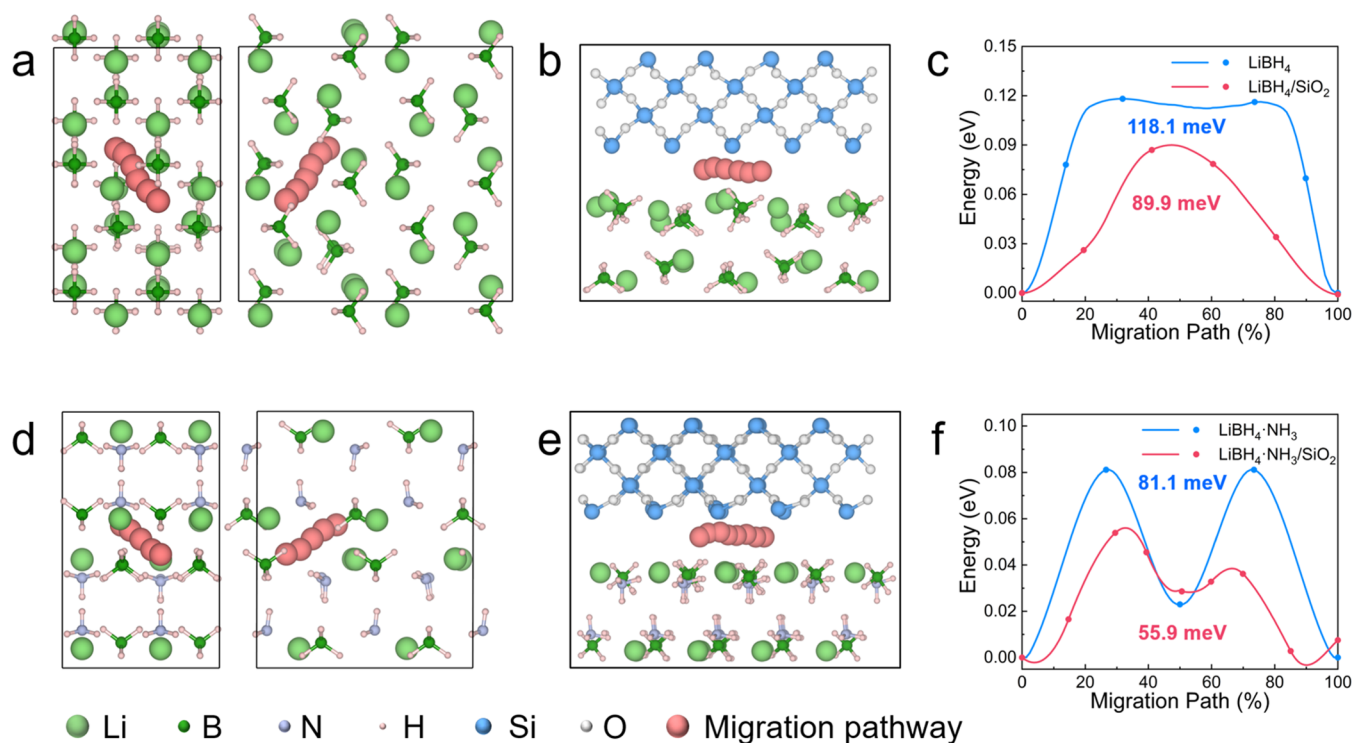**Figure 4.** Simulated migration pathway of interstitial Li in (a) $LiBH_4$, (b) $LiBH_4/SiO_2$, (d) $LiBH_4 \cdot NH_3$, and (e) $LiBH_4 \cdot NH_3/SiO_2$. (c, f) Corresponding energy curves.

distribution of Si and O elements inside the particle also ensures close contact with $Li(NH_3)_{0.2}BH_4$, which would help improve the ionic conductivity at the interface.

Further characterization of the interaction between $Li(NH_3)_xBH_4$ and SiO_2 was performed by X-ray photoelectron spectroscopy (XPS), as shown in Figure 2. Two states of the Li 1s spectrum of as-received $LiBH_4$ can be detected at 56.3 and 55.6 eV, respectively. The former binding energy is associated with the $Li–[BH_4]$ bond, whereas the latter is assigned to the $Li–O$ bond, mainly because of the transient air contamination of the sample surface during the measurement setting. In comparison, the relative intensity of the $Li–O$ bond visibly increases for both $LiBH_4@SiO_2$ and $Li(NH_3)_{0.2}BH_4@SiO_2$ composites, which suggests the interaction between $LiBH_4/$ $Li(NH_3)_{0.2}BH_4$ and SiO_2 via the $Li–O$ bond (Figure 2a). As shown in Figure 2b, similar results can be observed in the B 1s spectrum; the intensity of the $B–O$ bond becomes stronger with the addition of SiO_2, strongly indicating the active interface reaction between the complex hydride and fumed silica.[59] The binding of anionic groups can enhance the mobility of lithium ions.[40,41] Moreover, there is no significant difference in the spectrum of the samples containing SiO_2 before and after ammonia absorption (Figure 2c,d). Only the peak at 399.92 eV was attributed to the $N–H$ bond of $Li(NH_3)_{0.2}BH_4@SiO_2$, as observed in Figure 2e. This result is consistent with the EDS mapping (Figure 1g,h), which also suggests an effective absorption of ammonia molecules in the $LiBH_4$ structure.

Electrochemical Performance. The overall conductivity of the composites is presented according to the Arrhenius plot in Figures 3b and S3. The EIS plots of $Li(NH_3)_{0.2}BH_4@SiO_2$ using blocking electrodes (SUS/SUS) were also measured and are exhibited in Figure S4. It can be seen from the Arrhenius plots (Figure S3) of the $LiBH_4@SiO_2$ composites that the conductivity of the samples with 10, 30, and 50 wt % SiO_2 shows a small difference of 2.4×10^{-4}, 2.1×10^{-4}, and 1.9×10^{-4} S cm^{-1}, respectively. To obtain higher structural stability, the samples with 50 wt % SiO_2 were selected for subsequent ammonia absorption treatment. With an increasing amount of ammonia absorption ($x = 0$, 0.1, 0.2, 0.3, 0.4, and 0.5), the conductivity of the composites was drastically enhanced from 10^{-4} to 10^{-2} S cm^{-1}. The conductivities of $Li(NH_3)_xBH_4@$ SiO_2 with different ammonia contents were compared at 333 K (Figure 3c). The conductivity of $Li(NH_3)_{0.5}BH_4@SiO_2$ could reach 3.95×10^{-2} S cm^{-1}, 2 orders of magnitude higher than that of $LiBH_4@SiO_2$ (1.97×10^{-4} S cm^{-1}). This conductivity even exceeds those of other solid electrolytes such as hydride-based, oxide-based, sulfide-based, and halide-based solid electrolytes, as shown in Table S3. The higher lithium ionic conductivity is attributed to the crystal structure expansion with increased ammonia amount, thus resulting in an increased bulk conductivity. Furthermore, the enhancement of the conductivity after mixing with SiO_2 nanoparticles cannot be ignored. Many studies have been conducted to explore the mechanism of the significant improvement in conductivity between ionic conductors and insulating particles after ball-milling. One widely accepted theoretical model is the existence of a space charge layer at the intimate interface between the two phases.[60,61] In this space-charge layer, the ions overcome a smaller energy barrier and jump more frequently. The increased number of $Li–O$ and $B–O$ bonds in the XPS result provides direct evidence to support the concept of the space-charge layer. At low temperatures, the ionic conduction of the $Li(NH_3)_xBH_4@SiO_2$ composite electrolyte is controlled by the highly conductive interface. With increasing temperature, lithium ions are inclined to transfer in $Li(NH_3)_xBH_4$. Finally, a highly bulk phase and the conductive interface contribute to generating a large ion-diffusion channel.

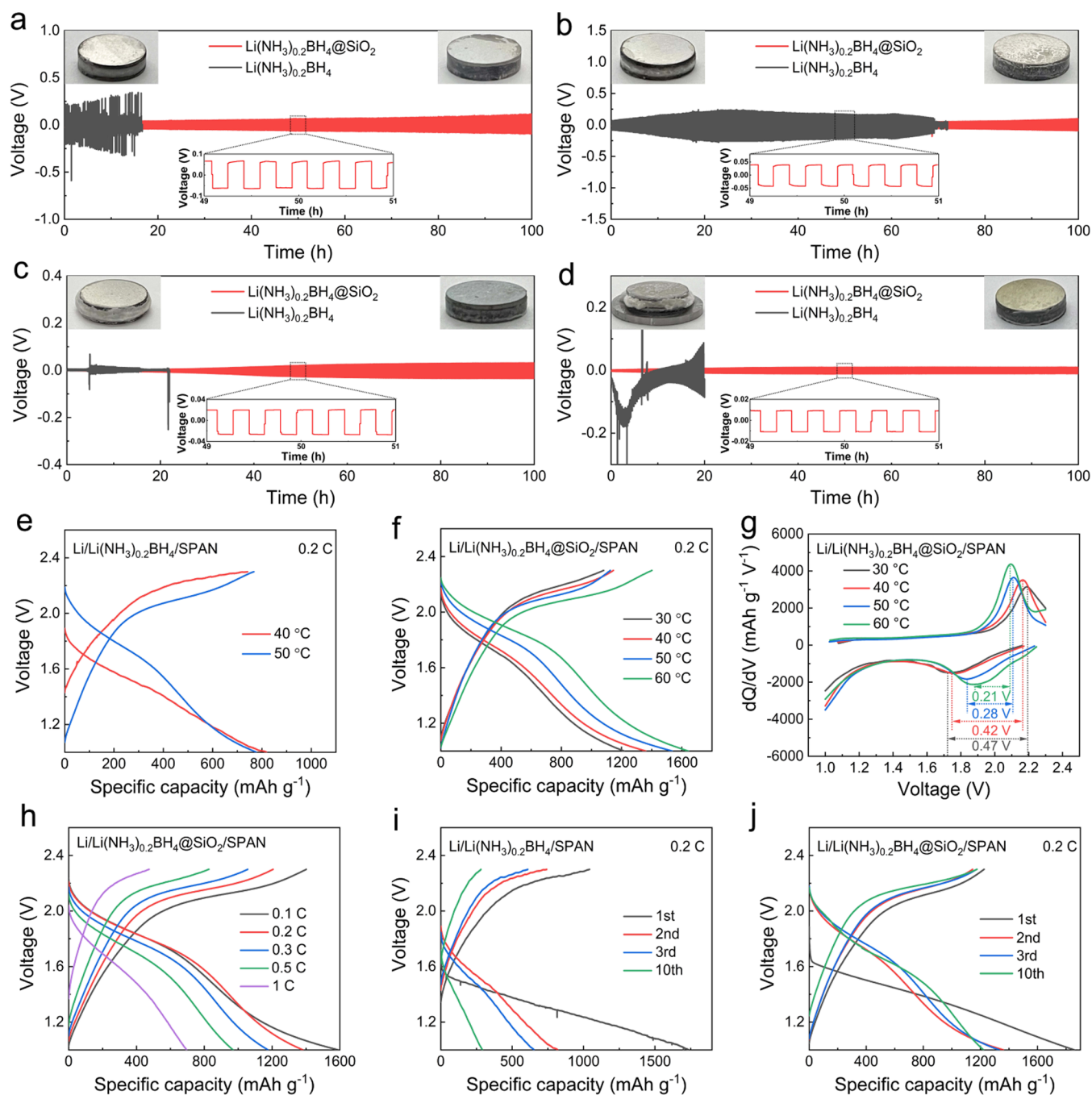**Figure 5.** Comparison of galvanostatic Li plating/stripping profiles of the Li/Li(NH$_3$)$_{0.2}$BH$_4$/Li and Li/Li(NH$_3$)$_{0.2}$BH$_4$@SiO$_2$/Li cells at 0.1 mA cm^{-2} at (a) 30 °C, (b) 40 °C, (c) 50 °C, and (d) 60 °C. Insets: digital images of Li/Li(NH$_3$)$_{0.2}$BH$_4$/Li (left) and Li/Li(NH$_3$)$_{0.2}$BH$_4$@SiO$_2$/Li (right) cells after cycles and prolonged galvanostatic cycling (bottom). (e, f) Galvanostatic charge/discharge curves (2nd cycle) of the Li/Li(NH$_3$)$_{0.2}$BH$_4$/SPAN and Li/Li(NH$_3$)$_{0.2}$BH$_4$@SiO$_2$/SPAN cells at different temperatures at 0.2C. (g) Differential capacitance curves of galvanostatic cycling curves of (f). (h) Rate performance of the Li/Li(NH$_3$)$_{0.2}$BH$_4$@SiO$_2$/SPAN cell at 40 °C at 0.1, 0.2, 0.3, 0.5, and 1C. (i, j) Galvanostatic charge/discharge curves of Li/Li(NH$_3$)$_{0.2}$BH$_4$/SPAN and Li/Li(NH$_3$)$_{0.2}$BH$_4$@SiO$_2$/SPAN cells at 40 °C and 0.2C, respectively.

It is generally acknowledged that low electronic conductivity plays a critical role in avoiding lithium dendrite formation in the solid electrolyte.[62] Figure 3d shows that the current decreases rapidly at first and then reaches a plateau after 3600 s under a potential of 500 mV using direct current (DC) polarization measurement at 303 K. The electronic conductivity of the Li(NH$_3$)$_{0.2}$BH$_4$@SiO$_2$ electrolyte is 3.4×10^{-9} S cm^{-1}, which is 5 orders of magnitude lower than that of Li$^+$ ionic conductivity. The lithium-ion transference number was determined to be 0.9999, which confirms Li ions as the major

charge carriers in the Li(NH$_3$)$_{0.2}$BH$_4$@SiO$_2$ composite.[38] Cyclic voltammetry (CV) was carried out to verify the electrochemical stability of SSE at a scanning rate of 1 mV s^{-1} from −0.5 to 2.4 V. It was observed that cathodic peaks related to lithium plating and anodic peaks related to lithium stripping appear close to 0 V versus Li/Li$^+$ on the stainless electrode, as shown in Figure 3e. There is no excess current peak because of electrolyte decomposition, implying that the Li(NH$_3$)$_{0.2}$BH$_4$@SiO$_2$ electrolyte is stable in the scan range from −0.5 to 2.4 V. To amplify the response current and accurately measure the

oxidation decomposition voltage of the $Li(NH_3)_{0.2}BH_4@SiO_2$ electrolyte, a Li/SSE/SSE + 25 wt % Super P/SUS cell was assembled for linear sweep voltammetry (LSV), as shown in Figure S5.[26] The results show that the oxidation decomposition voltage of the $Li(NH_3)_{0.2}BH_4@SiO_2$ electrolyte is 2.09 V. To evaluate the capability of the electrolyte to form lithium dendrites, galvanostatic cycling with increasing current density was performed at 50 °C (Figure 3f). The critical current density (CCD) of the $Li/Li(NH_3)_{0.2}BH_4@SiO_2/Li$ cell was determined to be 1.0 mA cm^{-2}.

Lithium-Ion Diffusion Mechanism. To understand the migration pathway of lithium ions, the diffusion behavior was simulated by DFT calculations. Orthorhombic $LiBH_4$ was utilized in the calculations. $LiBH_4 \cdot xNH_3$ was regarded as a mixture of $LiBH_4$ and $LiBH_4 \cdot NH_3$ in the molecular scale; $LiBH_4 \cdot NH_3$ was therefore selected to represent samples with different ammonia contents. Following the rules elucidated in the previous study that the interconnected metastable interstitial sites serve as the lowest energy path in $LiBH_4$,[63,64] only the formation and migration of interstitial Li (I_{Li}) were considered in this study. The migration of I_{Li} in $LiBH_4$ and $LiBH_4 \cdot NH_3$ was simulated first, as shown in Figure 4a,d. The calculated diffusion barrier of I_{Li} is 118.1 meV for $LiBH_4$ (Figure 4c) and 81.1 meV for $LiBH_4 \cdot NH_3$ (Figure 4f). These values are consistent with the previous report, demonstrating the excellent Li transport kinetics of these two solid-state electrolytes.[63] The enhanced diffusion kinetics of I_{Li} in $LiBH_4 \cdot NH_3$, which was reported in previous studies, is confirmed.[53] However, the formation energies (E_f) of I_{Li} in $LiBH_4$ and $LiBH_4 \cdot NH_3$ are as high as −0.16 and −0.24 eV, respectively. The high E_f hinders the appearance of I_{Li} and the subsequent diffusion process, which is believed to mainly account for the unsatisfactory Li ionic conductivity.[41,63]

After compositing $LiBH_4$ and $LiBH_4 \cdot NH_3$ with SiO_2, as illustrated in Figure 4b,e, the migrations of I_{Li} in the interlayers are simulated. The theoretical diffusion barriers are decreased to 89.9 and 55.9 meV in $LiBH_4/SiO_2$ and $LiBH_4 \cdot NH_3/SiO_2$, respectively. These results suggest that the Li transport dynamics in the interfacial space is more rapid than that in the crystal. Moreover, much lower E_f values of −1.91 and −1.95 eV are observed for I_{Li} in $LiBH_4/SiO_2$ and $LiBH_4 \cdot NH_3/SiO_2$, respectively, which indicates that the introduction of SiO_2 makes the I_{Li} easier to form in the interfacial region. An increase in the carrier concentration is very beneficial to the increase in conductivity. As a result, by introducing SiO_2 to form the composite, not only could the diffusion of Li be accelerated, but the formation of I_{Li} could also be promoted. All of these features contribute to the improved ionic conductivity of the $Li(NH_3)_xBH_4@SiO_2$ electrolyte.

Performance of ASSLBs. Considering the electrochemical stability window, low amount of ammonia, and high ionic conductivity of the electrolyte, $Li(NH_3)_{0.2}BH_4@SiO_2$ was chosen as the electrolyte to investigate the performance of ASSLBs. The stability of lithium metal with $Li(NH_3)_{0.2}BH_4@SiO_2$ was investigated as shown in Figure 5a−d. From the cycling plots of the symmetric cell, it was found that the $Li/Li(NH_3)_{0.2}BH_4/Li$ cell could not work properly because of the low ionic conductivity at low temperatures (30 and 40 °C) and electrolyte melting above 50 °C (Figure 5a−d, left digital photo). However, the charge−discharge curves of the symmetrical $Li/Li(NH_3)_{0.2}BH_4@SiO_2/Li$ cell at 0.1 mA cm^{-2} exhibits much better cycling with no short circuit after 100 h. The polarization potential is quite stable (60 mV at 30 °C,

38 mV at 40 °C, 26 mV at 50 °C, and 9 mV at 60 °C), and no fluctuation occurs from 100 h of cycling test at a current density of 0.1 mA cm^{-2}, revealing a stable interface with small interfacial resistance between the lithium metal and the electrolyte. Silica bricks can effectively suppress the melting problem of lithium borohydride ammoniates.

To further investigate the application prospect of the composite electrolyte in ASSLBs, the temperature adaptability, rate capability, and cycling performance of Li/SPAN cells were tested by galvanostatic charge−discharge experiments (Figure 5e−j). The discharge capacities of $Li/Li(NH_3)_{0.2}BH_4/SPAN$ cells at 0.2C are 818.7 mAh g^{-1} (40 °C, 2nd cycle) and 777 mAh g^{-1} (50 °C, 2nd cycle), respectively (Figure 5e). These cells also decayed or failed quickly within five cycles due to large polarization and structural instability. However, Figure 5f shows the discharge capacities of $Li/Li(NH_3)_{0.2}BH_4@SiO_2/SPAN$ cells at different temperatures at 0.2C. The discharge capacities are 1216.9 mAh g^{-1} (30 °C, 2nd cycle), 1361.2 mAh g^{-1} (40 °C, 2nd cycle), 1535.9 mAh g^{-1} (50 °C, 2nd cycle), and 1642.8 mAh g^{-1} (60 °C, 2nd cycle). The polarization potential decreased from 0.47 to 0.21 V when the temperature increased from 30 to 60 °C (Figure 5g). Moreover, when the current densities increase from 0.1, 0.2, 0.3, 0.5, and 1C in sequence at 40 °C, the specific capacities are 1589.8, 1381.9, 1176.0, 969.9, and 695.8 mAh g^{-1}, respectively, revealing a good rate performance of the ASSLBs fabricated with the SPAN and $Li(NH_3)_{0.2}BH_4@SiO_2$ electrolyte (Figure 5h). Besides, the full cell at 40 °C also exhibits specific discharge capacities of 1361.2 mAh g^{-1} (2nd cycle), 1331.6 mAh g^{-1} (3rd cycle), and 1221.7 mAh g^{-1} (10th cycle), with a high Coulombic efficiency close to 100%. However, the full cell without SiO_2 bricks shows rapid decay, with a discharge capacity of only 290.9 mAh g^{-1} at the 10th cycle (Figure 5i,j). The cycling performance was also tested at 0.1C and 60 °C, as shown in Figure S6. It yields a high capacity of 731.7 mAh g^{-1} with a Coulombic efficiency of 99.9% after 25 cycles. These results indicate that the composite material composed of lithium borohydride ammoniates ($Li(NH_3)_xBH_4$ as cement) and silicon dioxide (SiO_2 nanoparticles as bricks) can be applied as a solid-state electrolyte in all-solid-state lithium-ion batteries. In our future studies, we will continually improve the electrochemical performance of the full cell.

■ CONCLUSIONS

In summary, fast ionic electrolytes were obtained by introducing ammonia and nano-SiO_2 into $LiBH_4$. The highest ionic conductivity was 3.95×10^{-2} S cm^{-1} at 60 °C for the $Li(NH_3)_{0.5}BH_4@SiO_2$ composite. The absorption of ammonia makes the crystal structure of lithium borohydride expand or even change. The close interface between the borohydride and nano-SiO_2 will not only introduce a highly conductive layer but also enhance the stability of the macrostructure of the electrolyte. Based on these electrolytes, the assembled Li-SPAN solid-state batteries exhibit a high capacity of 1221.7 mAh g^{-1} at 0.2C and 40 °C after 10 cycles. The trial and application of solid-state electrolytes in full cells suggests that $Li(NH_3)_xBH_4@SiO_2$ is a promising SSE candidate for developing hydride-based ASSLBs with a high energy density.

■ EXPERIMENTAL METHODS

Material Synthesis and Structural Characterization. $LiBH_4$ (95%, Sigma-Aldrich), fumed SiO_2 (Aladdin), Li foil (China Energy Lithium Co. Ltd., Tianjin), and ammonia (NH_3 purity, 99.999%)

were used as received without further purification. The mixture with weight ratio compositions of $LiBH_4$–SiO_2 was mechanically milled at 400 rpm for 2 h with a planetary ball mill (Fritsch P7). The composite of $Li(NH_3)_xBH_4@SiO_2$ was prepared by introducing ammonia into $LiBH_4@SiO_2$ at room temperature. The quantification of ammonia was achieved by controlling the volume and pressure of ammonia in a closed container. Phase identification was achieved using a PANalytical Empyrean Multipurpose X-ray diffractometer with a copper Kα line. Samples for X-ray diffraction (XRD) analysis were prepared in a glovebox and sealed with Kapton films. For the in situ heating XRD characterization, the samples were measured at 5 °C per step with a heating rate of 5 °C min^{-1}. The samples stayed at each temperature for 20 min to achieve internal stability before testing. X-ray photoelectron spectroscopy (XPS) measurements were acquired with a Thermo Scientific K-Alpha+, XPS system, in which an Al Kα microfocus monochromatic source was employed. Transmission electron microscopy (TEM) observations and energy-dispersive X-ray spectroscopy (EDS) mapping were performed on a JEOL JEM-F200 coupled with JED-2300T.

Electrochemical Measurements and Characterization. The powder sample was loaded into stainless-steel vessels with 10 mm inner diameter and pressed into a pellet as the solid-state electrolyte. Two metallic lithium foils of 10 mm diameter were then placed on the two sides of the solid-state electrolyte as electrodes, forming a sandwich structure. All processes took place in the glovebox filled with Ar gas. Electrochemical impedance spectroscopy (EIS) measurements were implemented using a Bio-Logic SP-200 (France). The input frequency range was set to 7 MHz to 1 Hz. Experimental temperature ranges were set from 20 to 60 °C. The lithium ionic conductivity was evaluated from the diameter of the semicircle from the Nyquist plot. The lithium ionic conductivity is calculated by the following equation

$$\sigma = d/(S \times R) \tag{1}$$

where d, S, and R represent the thickness, surface area, and impedance of the electrolyte, respectively. The electronic conductivity (σ_e) was calculated according to the following relation

$$\sigma_e = I \times d/(U \times S) \tag{2}$$

where I is the steady-state current, U is the applied constant voltage, d is the thickness, and S is the area of the electrolyte pellet. The lithium-ion transference of SSE was calculated by the following equation

$$t^+ = 1 - \sigma_e/\sigma \tag{3}$$

in which σ_e and σ are the electronic conductivity and EIS conductivity, respectively. For the full cell, sulfurized polyacrylonitrile (SPAN) was used as the active material. Polyacrylonitrile and sulfur powder were mixed at a mass ratio of 1:4, and then an appropriate amount of absolute ethanol was added for mixing by ball-milling. After volatilization with the solvent, the mixed sample was heated in a nitrogen-filled tube furnace at 450 °C for 6 h to carbonize PAN and obtain the final product. The elemental composition of SPAN is shown in Figure S7, in which the S content accounts for 17.4 wt %. The composite cathode was prepared by the ball-milling of SPAN, Super-P, and $Li(NH_3)_{0.2}BH_4@SiO_2$ with a weight ratio of 30:10:60, respectively. The all-solid-state battery was assembled by pressing the composite cathode, SSE, and Li foil layer by layer. The electrochemical performance of the cells was measured by galvanostatic cycling (Land, China). The capacity is reported with respect to the mass of the active material.

Computational Method. Density functional theory (DFT) calculations were carried out by the projector-augmented wave (PAW) method as implemented in the Vienna ab initio simulation package (VASP).[65−68] A generalized gradient approximation (GGA) of the Perdew−Burke−Ernzerhof (PBE) functional was employed to describe the exchange−correlation interaction.[69] The van der Waals (vdW) correction DFT-D3 proposed by Grimme was chosen to describe the dispersion interaction.[70] The energy cutoff was set to 500 eV. The spin polarization and a $3 \times 3 \times 3$ γ centered k-point mesh were applied to all calculations. The structures were relaxed until the

forces and total energy on all atoms converged to less than 0.05 eV Å^{-1} and 1×10^{-5} eV. Diffusion barriers for Li hopping between adjacent interstitial sites in the crystal and interfacial region are calculated by the climbing-image nudged elastic band (CI-NEB) method.[71]

The formation energy (E_f) was calculated to evaluate the appearance of interstitial Li (I_{Li}) thermodynamically. E_f was defined as follows

$$E_f = E_{Li-SSE} - E_{SSE} - E_{Li}$$

where E_{Li-SSE} and E_{SSE} are the total energies of the solid-state electrolyte materials with and without I_{Li}, respectively, and E_{Li} is the energy of atomic Li. Therefore, a lower value of E_f indicates that I_{Li} is more likely to occur and the increase of carrier concentration.

■ ASSOCIATED CONTENT

ⓈI Supporting Information

The Supporting Information is available free of charge at https://pubs.acs.org/doi/10.1021/acsaem.2c02871.

> XRD pattern of fumed SiO_2; the calculated lattice spacing of $Li(NH_3)_xBH_4@SiO_2$; lattice parameters of $LiBH_4$ and $Li(NH_3)BH_4$; TEM images of fumed SiO_2 and $LiBH_4@SiO_2$; list of representative solid-state electrolytes and their conductivities; Arrhenius plots of $LiBH_4$-x wt % SiO_2; EIS plots of SUS/$Li(NH_3)_xBH_4@SiO_2$/SUS; LSV curve of $Li(NH_3)_xBH_4@SiO_2$; galvanostatic charge/discharge curves; and element weight content of SPAN (PDF)

■ AUTHOR INFORMATION

Corresponding Authors

Tengfei Zhang − Centre for Hydrogenergy, College of Materials Science and Technology, Nanjing University of Aeronautics and Astronautics, Nanjing 210016 Jiangsu, China; ⓞ orcid.org/0000-0002-9576-1093; Email: zhangtengfei@nuaa.edu.cn

Xuebin Yu − Department of Materials Science, Fudan University, Shanghai 200433, China; ⓞ orcid.org/0000-0002-4035-0991; Email: yuxuebin@fudan.edu.cn

Authors

Zhenhua Liu − Centre for Hydrogenergy, College of Materials Science and Technology, Nanjing University of Aeronautics and Astronautics, Nanjing 210016 Jiangsu, China

Shunlong Ju − Department of Materials Science, Fudan University, Shanghai 200433, China; ⓞ orcid.org/0000-0003-4342-0729

Yanda Ji − Department of Applied Physics, College of Physics and MIIT Key Laboratory of Aerospace Information Materials and Physics, Nanjing University of Aeronautics and Astronautics, Nanjing 211106 Jiangsu, China

Zhaotong Hu − Centre for Hydrogenergy, College of Materials Science and Technology, Nanjing University of Aeronautics and Astronautics, Nanjing 210016 Jiangsu, China

Yingtong Lv − Centre for Hydrogenergy, College of Materials Science and Technology, Nanjing University of Aeronautics and Astronautics, Nanjing 210016 Jiangsu, China

Guanglin Xia − Department of Materials Science, Fudan University, Shanghai 200433, China; ⓞ orcid.org/0000-0002-3493-4309

Complete contact information is available at:
https://pubs.acs.org/10.1021/acsaem.2c02871

■ **REFERENCES**

(1) Zou, Z.; Li, Y.; Lu, Z.; Wang, D.; Cui, Y.; Guo, B.; Li, Y.; Liang, X.; Feng, J.; Li, H.; Nan, C.-W.; Armand, M.; Chen, L.; Xu, K.; Shi, S. Mobile Ions in Composite Solids. *Chem. Rev.* **2020**, *120*, 4169−4221.

(2) Manthiram, A.; Yu, X.; Wang, S. Lithium Battery Chemistries Enabled by Solid-State Electrolytes. *Nat. Rev. Mater.* **2017**, *2*, 16103.

(3) Janek, J.; Zeier, W. G. A Solid Future for Battery Development. *Nat. Energy* **2016**, *1*, 16141.

(4) Pang, Y.; Nie, Z.; Xu, F.; Sun, L.; Yang, J.; Sun, D.; Fang, F.; Zheng, S. Borohydride Ammoniate Solid Electrolyte Design for All-Solid-State Mg Batteries. *Energy Environ. Mater.* **2022**, No. e12527.

(5) Shi, P.; Liu, Z.-Y.; Zhang, X.-Q.; Chen, X.; Yao, N.; Xie, J.; Jin, C.-B.; Zhan, Y.-X.; Ye, G.; Huang, J.-Q.; et al. Polar Interaction of Polymer Host−Solvent Enables Stable Solid Electrolyte Interphase in Composite Lithium Metal Anodes. *J. Energy Chem.* **2022**, *64*, 172−178.

(6) Zhang, T.; He, W.; Zhang, W.; Wang, T.; Li, P.; Sun, Z. M.; Yu, X. Designing Composite Solid-State Electrolytes for High Performance Lithium Ion or Lithium Metal Batteries. *Chem. Sci.* **2020**, *11*, 8686−8707.

(7) Chen, R.; Li, Q.; Yu, X.; Chen, L.; Li, H. Approaching Practically Accessible Solid-State Batteries: Stability Issues Related to Solid Electrolytes and Interfaces. *Chem. Rev.* **2020**, *120*, 6820−6877.

(8) Pang, Y.; Pan, J.; Yang, J.; Zheng, S.; Wang, C. Electrolyte/Electrode Interfaces in All-Solid-State Lithium Batteries: A Review. *Electrochem. Energy Rev.* **2021**, *4*, 169−193.

(9) Masquelier, C. Solid Electrolytes: Lithium Ions on the Fast Track. *Nat. Mater.* **2011**, *10*, 649−650.

(10) Xiao, Y.; Turcheniuk, K.; Narla, A.; Song, A. Y.; Ren, X.; Magasinski, A.; Jain, A.; Huang, S.; Lee, H.; Yushin, G. Electrolyte Melt Infiltration for Scalable Manufacturing of Inorganic All-Solid-State Lithium-Ion Batteries. *Nat. Mater.* **2021**, *20*, 984−990.

(11) Lin, Y.; Wu, M.; Sun, J.; Zhang, L.; Jian, Q.; Zhao, T. A High-Capacity, Long-Cycling All-Solid-State Lithium Battery Enabled by Integrated Cathode/Ultrathin Solid Electrolyte. *Adv. Energy Mater.* **2021**, *11*, No. 2101612.

(12) Zhang, X.; Zhang, T.; Shao, Y.; Cao, H.; Liu, Z.; Wang, S.; Zhang, X. Composite Electrolytes Based on Poly(Ethylene Oxide) and Lithium Borohydrides for All-Solid-State Lithium-Sulfur Batteries. *ACS Sustainable Chem. Eng.* **2021**, *9*, 5396−5404.

(13) Pang, Q.; Zhou, L.; Nazar, L. F. Elastic and Li-Ion−Percolating Hybrid Membrane Stabilizes Li Metal Plating. *Proc. Natl. Acad. Sci. U.S.A.* **2018**, *115*, 12389−12394.

(14) Jinisha, B.; Anilkumar, K. M.; Manoj, M.; Pradeep, P.; Jayalekshmi, J. Development of a Novel Type of Solid Polymer Electrolyte for Solid State Lithium Battery Applications Based on Lithium Enriched Poly (Ethylene Oxide) (PEO)/Poly (Vinyl Pyrrolidone) (PVP) Blend Polymer. *Electrochim. Acta* **2017**, *235*, 210−222.

(15) Lin, D.; Liu, W.; Liu, Y.; Lee, H. R.; Hsu, P. C.; Liu, K.; Cui, Y. High Ionic Conductivity of Composite Solid Polymer Electrolyte via in Situ Synthesis of Monodispersed SiO_2 Nanospheres in Poly-(Ethylene Oxide). *Nano Lett.* **2016**, *16*, 459−465.

(16) Li, H.; Du, Y.; Wu, X.; Xie, J.; Lian, F. Developing "Polymer-in-Salt" High Voltage Electrolyte Based on Composite Lithium Salts for Solid-State Li Metal Batteries. *Adv. Funct. Mater.* **2021**, *31*, No. 2103049.

(17) Anantharamulu, N.; Koteswara Rao, K.; Rambabu, G.; Vijaya Kumar, B.; Radha, V.; Vithal, M. A Wide-Ranging Review on Nasicon Type Materials. *J. Mater. Sci.* **2011**, *46*, 2821−2837.

(18) Stramare, S.; Thangadurai, V.; Weppner, W. Lithium Lanthanum Titanates: A Review. *Chem. Mater.* **2003**, *15*, 3974−3990.

(19) Yu, K.; Gu, R.; Wu, L.; Sun, H.; Ma, R.; Jin, L.; Xu, Y.; Xu, Z.; Wei, X. Ionic and Electronic Conductivity of Solid Electrolyte $Li_{0.5}La_{0.5}TiO_3$ Doped with LiO_2-SiO_2-B_2O_3 Glass. *J. Alloys Compd.* **2018**, *739*, 892−896.

(20) Fu, J.; Yu, P.; Zhang, N.; Ren, G.; Zheng, S.; Huang, W.; Long, X.; Li, H.; Liu, X. In Situ Formation of a Bifunctional Interlayer Enabled by a Conversion Reaction to Initiatively Prevent Lithium Dendrites in a Garnet Solid Electrolyte. *Energy Environ. Sci.* **2019**, *12*, 1404−1412.

(21) Puente, P. M. G.; Song, S.; Cao, S.; Rannalter, L. Z.; Pan, Z.; Xiang, X.; Shen, Q.; Chen, F. Garnet-Type Solid Electrolyte: Advances of Ionic Transport Performance and Its Application in All-Solid-State Batteries. *J. Adv. Ceram.* **2021**, *10*, 933−972.

(22) Kudu, Ö. U.; Famprikis, T.; Fleutot, B.; Braida, M. D.; le Mercier, T.; Islam, M. S.; Masquelier, C. A Review of Structural Properties and Synthesis Methods of Solid Electrolyte Materials in the $Li_2S − P_2S_5$ Binary System. *J. Power Sources* **2018**, *407*, 31−43.

(23) Kato, Y.; Hori, S.; Saito, T.; Suzuki, K.; Hirayama, M.; Mitsui, A.; Yonemura, M.; Iba, H.; Kanno, R. High-Power All-Solid-State Batteries Using Sulfide Superionic Conductors. *Nat. Energy* **2016**, *1*, 16030.

(24) Lian, P. J.; Zhao, B. S.; Zhang, L. Q.; Xu, N.; Wu, M. T.; Gao, X. P. Inorganic Sulfide Solid Electrolytes for All-Solid-State Lithium Secondary Batteries. *J. Mater. Chem. A* **2019**, *7*, 20540−20557.

(25) Tan, D. H. S.; Yu-Ting, C.; Hedi, Y.; Wurigumula, B.; Bhagath, S.; Jean-Marie, D.; Weikang, L.; Bingyu, L.; So-Yeon, H.; Baharak, S.; Jonathan, S.; Wu, E. A.; Grayson, D.; Eun, H. H.; Jin, H. H.; Hyeri, J.; Beom, L. J.; Zheng, C.; Shirley, M. Y. Carbon-Free High-Loading Silicon Anodes Enabled by Sulfide Solid Electrolytes. *Science* **2021**, *373*, 1494−1499.

(26) Zhang, T.; Shao, Y.; Zhang, X.; Huang, Y.; Wang, S.; Zhou, W.; Li, P.; Xia, G.; Yu, X. Fast Lithium Ionic Conductivity in Complex Hydride-Sulfide Electrolytes by Double Anions Substitution. *Small Methods* **2021**, *5*, No. 2100609.

(27) Fu, Z.-H.; Chen, X.; Yao, N.; Shen, X.; Ma, X.-X.; Feng, S.; Wang, S.; Zhang, R.; Zhang, L.; Zhang, Q. The Chemical Origin of Temperature-Dependent Lithium-Ion Concerted Diffusion in Sulfide Solid Electrolyte $Li_{10}GeP_2S_{12}$. *J. Energy Chem.* **2022**, *70*, 59−66.

(28) Zhang, Y.; Zhan, L.; Zhuang, X.; Zhu, Y.; Wan, N.; Guo, X.; Chen, J.; Wang, Z.; Li, L. The Ionic Conductivities, Stabilities and Ionic Mobilities of $xLiBH_4$-Li_2NH (x = 1, 2, 4) Composites as Fast Ion Conductor. *J. Alloys Compd.* **2017**, *695*, 2894−2901.

(29) Blanchard, D.; Nale, A.; Sveinbjörnsson, D.; Eggenhuisen, T. M.; Verkuijlen, M. H. W.; Suwarno; Vegge, T.; Kentgens, A. P. M.; de Jongh, P. E. Nanoconfined $LiBH_4$ as a Fast Lithium Ion Conductor. *Adv. Funct. Mater.* **2015**, *25*, 184−192.

(30) Gulino, V.; Brighi, M.; Dematteis, E. M.; Murgia, F.; Nervi, C.; Černý, R.; Baricco, M. Phase Stability and Fast Ion Conductivity in the Hexagonal $LiBH_4$−$LiBr$−$LiCl$ Solid Solution. *Chem. Mater.* **2019**, *31*, 5133−5144.

(31) Unemoto, A.; Chen, C.; Wang, Z.; Matsuo, M.; Ikeshoji, T.; Orimo, S. Pseudo-Binary Electrolyte, $LiBH_4$−$LiCl$, for Bulk-Type All-Solid-State Lithium-Sulfur Battery. *Nanotechnology* **2015**, *26*, No. 254001.

(32) Maekawa, H.; Matsuo, M.; Takamura, H.; Ando, M.; Noda, Y.; Karahashi, T.; Orimo, S. Halide-Stabilized $LiBH_4$, a Room-Temperature Lithium Fast-Ion Conductor. *J. Am. Chem. Soc.* **2009**, *131*, 894−895.

(33) Shi, X.; Pang, Y.; Wang, B.; Sun, H.; Wang, X.; Li, Y.; Yang, J.; Li, H.-W.; Zheng, S. In Situ Forming LiF Nanodecorated Electrolyte/

Electrode Interfaces for Stable All-Solid-State Batteries. *Mater. Today Nano* **2020**, *10*, No. 100079.

(34) Li, X.; Liang, J.; Chen, N.; Luo, J.; Adair, K. R.; Wang, C.; Banis, M. N.; Sham, T.; Zhang, L.; Zhao, S.; Lu, S.; Huang, H.; Li, R.; Sun, X. Water-Mediated Synthesis of a Superionic Halide Solid Electrolyte. *Angew. Chem.* **2019**, *131*, 16579−16584.

(35) Dondelinger, M.; Swanson, J.; Nasymov, G.; Jahnke, C.; Qiao, Q.; Wu, J.; Widener, C.; Numan-Al-Mobin, A. M.; Smirnova, A. Electrochemical Stability of Lithium Halide Electrolyte with Antiperovskite Crystal Structure. *Electrochim. Acta* **2019**, *306*, 498−505.

(36) Asano, T.; Sakai, A.; Ouchi, S.; Sakaida, M.; Miyazaki, A.; Hasegawa, S. Solid Halide Electrolytes with High Lithium-Ion Conductivity for Application in 4 V Class Bulk-Type All-Solid-State Batteries. *Adv. Mater.* **2018**, *30*, No. 1803075.

(37) Tanibata, N.; Takimoto, S.; Nakano, K.; Takeda, H.; Nakayama, M.; Sumi, H. Metastable Chloride Solid Electrolyte with High Formability for Rechargeable All-Solid-State Lithium Metal Batteries. *ACS Mater. Lett.* **2020**, *2*, 880−886.

(38) Wang, C.; Liang, J.; Luo, J.; Liu, J.; Li, X.; Zhao, F.; Li, R.; Huang, H.; Zhao, S.; Zhang, L.; Wang, J.; Sun, X. A Universal Wet-Chemistry Synthesis of Solid-State Halide Electrolytes for All-Solid-State Lithium-Metal Batteries. *Sci. Adv.* **2021**, *7*, No. eabh1896.

(39) Zhu, M.; Pang, Y.; Lu, F.; Shi, X.; Yang, J.; Zheng, S. In Situ Formed Li-B-H Complex with High Li-Ion Conductivity as a Potential Solid Electrolyte for Li Batteries. *ACS Appl. Mater. Interfaces* **2019**, *11*, 14136−14141.

(40) Ngene, P.; Lambregts, S. F. H.; Blanchard, D.; Vegge, T.; Sharma, M.; Hagemann, H.; de Jongh, P. E. The Influence of Silica Surface Groups on the Li-Ion Conductivity of LiBH$_4$/SiO$_2$ Nanocomposites. *Phys. Chem. Chem. Phys.* **2019**, *21*, 22456−22466.

(41) Choi, Y. S.; Lee, Y. S.; Choi, D. J.; Chae, K. H.; Oh, K. H.; Cho, Y. W. Enhanced Li Ion Conductivity in LiBH$_4$-Al$_2$O$_3$ Mixture via Interface Engineering. *J. Phys. Chem. C* **2017**, *121*, 26209−26215.

(42) Lefevr, J.; Cervini, L.; Griffin, J. M.; Blanchard, D. Lithium Conductivity and Ions Dynamics in LiBH$_4$/SiO$_2$ Solid Electrolytes Studied by Solid-State NMR and Quasi-Elastic Neutron Scattering and Applied in Lithium-Sulfur Batteries. *J. Phys. Chem. C* **2018**, *122*, 15264−15275.

(43) Liu, Z.; Xiang, M.; Zhang, Y.; Shao, H.; Zhu, Y.; Guo, X.; Li, L.; Wang, H.; Liu, W. Lithium Migration Pathways at the Composite Interface of LiBH$_4$ and Two-Dimensional MoS$_2$ Enabling Superior Ionic Conductivity at Room Temperature. *Phys. Chem. Chem. Phys.* **2020**, *22*, 4096−4105.

(44) Choi, Y. S.; Lee, Y. S.; Oh, K. H.; Cho, Y. W. Interface-Enhanced Li Ion Conduction in a LiBH$_4$-SiO$_2$ Solid Electrolyte. *Phys. Chem. Chem. Phys.* **2016**, *18*, 22540−22547.

(45) Gulino, V.; Barberis, L.; Ngene, P.; Baricco, M.; de Jongh, P. E. Enhancing Li-Ion Conductivity in LiBH$_4$-Based Solid Electrolytes by Adding Various Nanosized Oxides. *ACS Appl. Energy Mater.* **2020**, *3*, 4941−4948.

(46) Epp, V.; Wilkening, M. Motion of Li+ in Nanoengineered LiBH$_4$ and LiBH$_4$:Al$_2$O$_3$ Comparison with the Microcrystalline Form. *ChemPhysChem* **2013**, *14*, 3706−3713.

(47) Unemoto, A.; Wu, H.; Udovic, T. J.; Matsuo, M.; Ikeshoji, T.; Orimo, S. I. Fast Lithium-Ionic Conduction in a New Complex Hydride-Sulphide Crystalline Phase. *Chem. Commun.* **2016**, *52*, 564−566.

(48) Zhan, L.; Zhang, Y.; Zhuang, X.; Fang, H.; Zhu, Y.; Guo, X.; Chen, J.; Wang, Z.; Li, L. Ionic Conductivities of Lithium Borohydride-Lithium Nitride Composites. *Solid State Ionics* **2017**, *304*, 150−155.

(49) Suwarno; Ngene, P.; Nale, A.; Eggenhuisen, T. M.; Oschatz, M.; Embs, J. P.; Remhof, A.; de Jongh, P. E. Confinement Effects for Lithium Borohydride: Comparing Silica and Carbon Scaffolds. *J. Phys. Chem. C* **2017**, *121*, 4197−4205.

(50) de Kort, L. M.; Harmel, J.; de Jongh, P. E.; Ngene, P. The Effect of Nanoscaffold Porosity and Surface Chemistry on the Li-Ion Conductivity of LiBH$_4$-LiNH$_2$/Metal Oxide Nanocomposites. *J. Mater. Chem. A* **2020**, *8*, 20687−20697.

(51) Liu, H.; Jiao, L.; Zhao, Y.; Cao, K.; Liu, Y.; Wang, Y.; Yuan, H. Improved Dehydrogenation Performance of LiBH$_4$ by Confinement into Porous TiO$_2$ Micro-Tubes. *J. Mater. Chem. A* **2014**, *2*, 9244−9250.

(52) Lu, F.; Pang, Y.; Zhu, M.; Han, F.; Yang, J.; Fang, F.; Sun, D.; Zheng, S.; Wang, C. A High-Performance Li−B−H Electrolyte for All-Solid-State Li Batteries. *Adv. Funct. Mater.* **2019**, *29*, No. 1809219.

(53) Zhang, T.; Wang, Y.; Song, T.; Miyaoka, H.; Shinzato, K.; Miyaoka, H.; Ichikawa, T.; Shi, S.; Zhang, X.; Isobe, S.; Hashimoto, N.; Kojima, Y. Ammonia, a Switch for Controlling High Ionic Conductivity in Lithium Borohydride Ammoniates. *Joule* **2018**, *2*, 1522−1533.

(54) Johnson, S. R.; David, W. I. F.; Royse, D. M.; Sommariva, M.; Tang, C. Y.; Fabbiani, F. P. A.; Jones, M. O.; Edwards, P. P. The Monoammoniate of Lithium Borohydride, Liachtungtrenung Li-(NH$_3$)BH$_4$: An Effective Ammonia Storage Compound. *Chem. − Asian J.* **2009**, *4*, 849−854.

(55) Yan, Y.; Grinderslev, J. B.; Lee, Y. S.; Jørgensen, M.; Cho, Y. W.; Černý, R.; Jensen, T. R. Ammonia-Assisted Fast Li-Ion Conductivity in a New Hemiammine Lithium Borohydride, LiBH$_4$·1/2NH$_3$. *Chem. Commun.* **2020**, *56*, 3971−3974.

(56) Zhang, R.; Li, H.; Wang, Q.; Wei, S.; Yan, Y.; Chen, Y. Size Effect of MgO on the Ionic Conduction Properties of a LiBH$_4$·1/2NH$_3$−MgO Nanocomposite. *ACS Appl. Mater. Interfaces* **2022**, *14*, 8947−8954.

(57) Guo, Y.; Xia, G.; Zhu, Y.; Gao, L.; Yu, X. Hydrogen Release from Amminelithium Borohydride, LiBH$_4$· NH$_3$. *Chem. Commun.* **2010**, *46*, 2599−2601.

(58) Breuer, S.; Pregartner, V.; Lunghammer, S.; Wilkening, H. M. R. Dispersed Solid Conductors: Fast Interfacial Li-Ion Dynamics in Nanostructured LiF and LiF γ-Al$_2$O$_3$ Composites. *J. Phys. Chem. C* **2019**, *123*, 5222−5230.

(59) Zhang, R.; Zhao, W.; Liu, Z.; Wei, S.; Yan, Y.; Chen, Y. Enhanced Room Temperature Ionic Conductivity of the LiBH$_4$·1/2NH$_3$-Al$_2$O$_3$composite. *Chem. Commun.* **2021**, *57*, 2380−2383.

(60) Roman, H. E. A Continuum Percolation Model for Dispersed Ionic Conductors. *J. Phys.: Condens. Matter* **1990**, *2*, 3909−3917.

(61) Agrawal, R. C.; Gupta, R. K. Superionic Solid: Composite Electrolyte Phase − an Overview. *J. Mater. Sci.* **1999**, *34*, 1131−1162.

(62) Han, F.; Westover, A. S.; Yue, J.; Fan, X.; Wang, F.; Chi, M.; Leonard, D. N.; Dudney, N. J.; Wang, H.; Wang, C. High Electronic Conductivity as the Origin of Lithium Dendrite Formation within Solid Electrolytes. *Nat. Energy* **2019**, *4*, 187−196.

(63) Lee, Y. S.; Cho, Y. W. Fast Lithium Ion Migration in Room Temperature LiBH$_4$. *J. Phys. Chem. C* **2017**, *121*, 17773−17779.

(64) Zettl, R.; Hogrefe, K.; Gadermaier, B.; Hanzu, I.; Ngene, P.; de Jongh, P. E.; Wilkening, H. M. R. Conductor-Insulator Interfaces in Solid Electrolytes: A Design Strategy to Enhance Li-Ion Dynamics in Nanoconfined LiBH$_4$/Al$_2$O$_3$. *J. Phys. Chem. C* **2021**, *125*, 15052−15060.

(65) Kresse, G.; Furthmüller, J. Efficiency of Ab-Initio Total Energy Calculations for Metals and Semiconductors Using a Plane-Wave Basis Set. *Comput. Mater. Sci.* **1996**, *6*, 15−50.

(66) Kresse, G.; Hafner, J. Ab Initio Molecular-Dynamics Simulation of the Liquid-Metalamorphous- Semiconductor Transition in Germanium. *Phys. Rev. B* **1994**, *49*, 14251−14269.

(67) Blöchl, P. E. Projector Augmented-Wave Method. *Phys. Rev. B* **1994**, *50*, 17953−17979.

(68) Kresse, G.; Joubert, D. From Ultrasoft Pseudopotentials to the Projector Augmented-Wave Method. *Phys. Rev. B* **1999**, *59*, 1758.

(69) Perdew, J. P.; Burke, K.; Ernzerhof, M. Generalized Gradient Approximation Made Simple. *Phys. Rev. Lett.* **1996**, *77*, 3865−3868.

(70) Grimme, S.; Antony, J.; Ehrlich, S.; Krieg, H. A Consistent and Accurate Ab Initio Parametrization of Density Functional Dispersion Correction (DFT-D) for the 94 Elements H-Pu. *J. Chem. Phys.* **2010**, *132*, No. 154104.

(71) Heyden, A.; Bell, A. T.; Keil, F. J. Efficient Methods for Finding Transition States in Chemical Reactions: Comparison of Improved Dimer Method and Partitioned Rational Function Optimization Method. *J. Chem. Phys.* **2005**, *123*, No. 224101.

📖 Recommended by ACS